# Dynamics of the Conformational Transitions in the Assembling of the Michaelis Complex of a Bisubstrate Enzyme: A $^{15}$N Relaxation Study of *Escherichia coli* 6-Hydroxymethyl-7,8-dihydropterin Pyrophosphokinase[†]

Ewen Lescop,[‡,§] Zhenwei Lu,[||] Qin Liu,[||,⊥] Huimin Xu,[‡,#] Guangyu Li,[||,▽] Bin Xia,[‡,#,○] Honggao Yan,*[,||] and Changwen Jin*[,‡,#,○]

*Beijing NMR Center, College of Life Sciences, and College of Chemistry and Molecular Engineering, Peking University, Beijing 100871, China, and Department of Biochemistry and Molecular Biology, Michigan State University, East Lansing, Michigan 48824*

*Received August 27, 2008; Revised Manuscript Received November 24, 2008*

ABSTRACT: 6-Hydroxymethyl-7,8-dihydropterin pyrophosphokinase (HPPK) catalyzes the transfer of pyrophosphate from ATP to 6-hydroxymethyl-7,8-dihydropterin (HP), which follows an ordered bi-bi kinetic mechanism with ATP binding to the enzyme first. HPPK undergoes dramatic conformational changes during its catalytic cycle as revealed by X-ray crystallography, and the conformational changes are essential for the enzymatic catalysis as shown by site-directed mutagenesis and biochemical and crystallographic analysis of the mutants. However, the dynamic properties of the enzyme have not been measured experimentally. Here, we report a $^{15}$N NMR relaxation study of the dynamic properties of *Escherichia coli* HPPK from the apo form to the binary substrate complex with MgATP (represented by MgAMPCPP, an ATP analogue) to the Michaelis complex (ternary substrate complex) with MgATP (represented by MgAMPCPP) and HP (represented by 7,7-dimethyl-6-hydroxypterin, an HP analogue). The results show that the binding of the nucleotide to HPPK does not cause major changes in the dynamic properties of the enzyme. Whereas enzymes are often more rigid when bound to the ligand or the substrate, the internal mobility of HPPK is not reduced and is even moderately increased in the binary complex, particularly in the catalytic loops. The internal mobility of the catalytic loops is significantly quenched upon the formation of the ternary complex, but some mobility remains. The enhanced motions in the catalytic loops of the binary substrate complex may be required for the assembling of the ternary complex. On the other hand, some degrees of mobility in the catalytic loops of the ternary complex may be required for the optimal stabilization of the transition state, which may need the instantaneous adjustment and alignment of the side-chain positions of catalytic residues. Such dynamic behaviors may be characteristic of bisubstrate enzymes.

6-Hydroxymethyl-7,8-dihydropterin pyrophosphokinase (HPPK)[1] catalyzes the transfer of pyrophosphate from ATP to 6-hydroxymethyl-7,8-dihydropterin (HP, Figure 1a), leading to the biosynthesis of folate cofactors (*1*). Folate cofactors are essential for life (*2*). Mammals have an active transport system for deriving folates from the diet. In contrast, most microorganisms must synthesize folates *de novo*, because they lack the active transport system. Therefore, like other enzymes in the folate biosynthetic pathway, HPPK is an attractive target for developing antimicrobial agents.

Protein dynamics is thought to play an important role in enzymatic catalysis (*3*−*7*). While the role of protein dynamics in the chemical step of bond cleavage and formation is still controversial (*8, 9*), it is no doubt that protein dynamics plays an important role in the physical steps of the assembling of the Michaelis complex and product release. Although structural studies have provided ample evidence for protein conformational changes through a catalytic cycle, there are only a few systematic experimental studies of the dynamic properties of enzymes through their catalytic cycles and their roles in the conformational transitions that are required for enzymatic catalysis (see ref *4* for an excellent recent review). Our understanding of the role of protein

[†] This work was supported in part by NIH Grant GM58221 to H.Y. and Grants 2006AA02A323 from the National High Technology Research and Development Program of China and 2006CB910203 from the National Basic Research Program of China to C.J. E.L. acknowledges a fellowship from the Sino-French Foundation for Science and Its Applications (FFCSA). This study made use of NMR spectrometers at Beijing NMR Center (Peking University) and a Varian INOVA-600 NMR spectrometer at Michigan State University funded in part by NSF Grant BIR9512253.

* Corresponding authors. H.Y.: tel, (517) 353-8786; fax, (517) 353-9334; e-mail, yanh@msu.edu. C.J.: tel, 86-10-6275-6004; fax, 86-10-6275-3790; e-mail, changwen@pku.edu.cn.

[‡] Beijing NMR Center, Peking University.

[§] Current address: Laboratoire de Chimie et Biologie Structurales, ICSN-CNRS, 1, avenue de la Terrasse, 91190 Gif-sur-Yvette, France.

[||] Department of Biochemistry and Molecular Biology, Michigan State University.

[⊥] Current address: Biomolecular NMR Laboratory, The University of Western Ontario, London, Ontario, Canada N6A 5C1.

[#] College of Life Sciences, Peking University.

[▽] Current address: NMR Facility, Shanghai Institute of Organic Chemistry, Chinese Academy of Sciences, 354 Fenglin Lu, Shanghai 200032, China.

[○] College of Chemistry and Molecular Engineering, Peking University.

[1] Abbreviations: AMPCPP, α,β-methyleneadenosine triphosphate; CPMG, Carr−Purcell−Meiboom−Gill; DMHP, 7,7-dimethyl-6-hydroxypterin; HP, 6-hydroxymethyl-7,8-dihydropterin; HPPK, 6-hydroxymethyl-7,8-dihydropterin pyrophosphokinase; HPPP, 6-hydroxymethyl-7,8-dihydropterin pyrophosphate; HSQC, heteronuclear single-quantum coherence; IPTG, isopropyl β-D-thiogalactoside; NOE, nuclear Overhauser effect; $\tau_c$, correlation time.

10.1021/bi8016262 CCC: $40.75 
Published on Web 12/24/2008

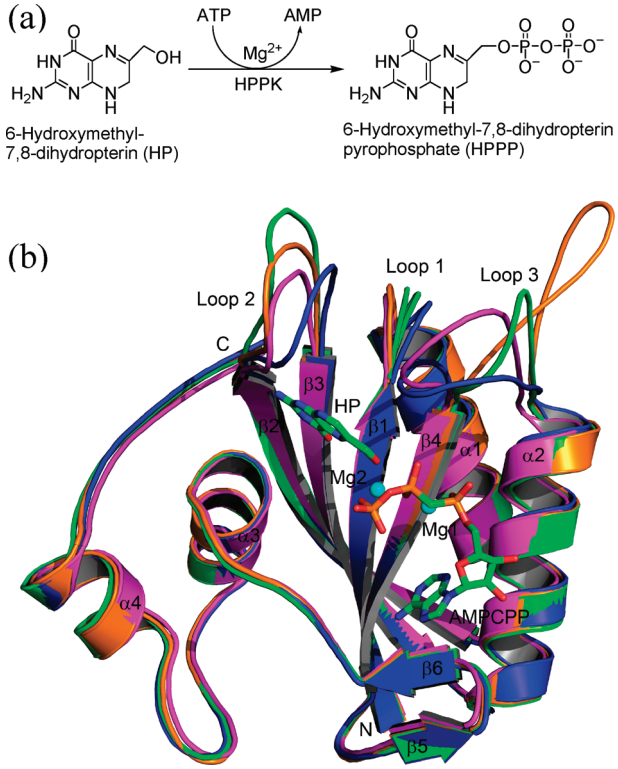


FIGURE 1: The HPPK-catalyzed reaction (a) and a ribbon diagram of the crystal structures of HPPK showing the conformational changes of the three catalytic loops during several stages of its catalytic cycle (b). The apoenzyme (PDB code 1HKA) is in green, the ternary substrate complex (PDB code 1Q0N) with HP, AMPCPP (a substrate ATP analogue), and $Mg^{2+}$ in blue, the ternary product complex (PDB code 1RAO) with HPPP and AMP in orange, and the binary product complex (PDB code 1RB0) with HPPP in magenta. Loop 1 of the apoenzyme has two conformations. AMPCPP, HP, and two $Mg^{2+}$ ions are drawn to illustrate the location of the active center. Panel b was made with PyMOL (*45*).

dynamics in enzymatic catalysis lags far behind our knowledge of the structures and chemical mechanisms of enzymes. With great progress in structural genomics and structure−function relationship studies, elucidating the role of protein dynamics in enzymatic catalysis becomes one of the greatest remaining challenges for biochemists and biophysicists. *Escherichia coli* HPPK has emerged as an excellent model for studying the role of protein dynamics in enzymatic catalysis, because the enzyme is small (~18 kDa), stable, and amenable to both X-ray crystallographic and NMR analysis. Atomic structures have been determined for nearly every stage of the catalytic cycle, and protein dynamics has been shown to be important for HPPK catalysis (*10*−*24*).

The HPPK-catalyzed reaction follows an ordered kinetic mechanism with ATP binding to the enzyme first (*15, 18*). Comparative analysis of the crystal structures of ligand-free HPPK and its ternary complex has revealed that the complete active center of HPPK is assembled only after both substrates bind to the enzyme (*14, 21*). The assembling of the active center involves large conformational changes, particularly in the three catalytic loops (Figure 1b). Of the three catalytic loops, loop 3 undergoes most dramatic conformational changes. As expected, the loop moves in to close the active center upon the formation of the ternary complex (*14*). However, the loop moves away from the active center upon the binding of MgADP or an MgATP analogue (*16*). Recently, it has been shown that loop 3 also moves away from the active center upon the completion of pyrophosphoryl transfer, to the same extent as upon the binding of MgADP or an MgATP analogue (*21*). By site-directed mutagenesis, it has been shown that loop 3 is required for the assembly of the full active center, plays an important role in the stabilization of the ternary complex and the transition state of the reaction, and is essential for catalysis (*22, 23*).

While the crystal and NMR structures have provided the snapshots of the catalytic cycle, the dynamic properties of HPPK at various stages of the catalytic cycle have to be studied, in order to fully understand the relationship between protein dynamics and catalysis in HPPK. In the present work, we investigate the backbone dynamic properties of *E. coli* HPPK by $^{15}N$ relaxation measurements focusing on the assembling of the Michaelis complex, i.e., from the apoenzyme to the binary substrate complex to the ternary Michaelis complex. Model-free analysis of the $^{15}N$ NMR relaxation data together with the weak or missing signals from loop 3 revealed that the three catalytic loops are mobile at different time scales in the absence of ligand. Surprisingly, the binding of the nucleotide to HPPK does not cause major changes in the dynamic properties of the enzyme. Whereas enzymes are often more rigidified upon the binding of a substrate or a ligand, the internal mobility of HPPK is not reduced and is even moderately increased in the binary complex, particularly in the catalytic loops. The enhanced motions in the three loops may be required for the assembling of the ternary substrate complex. The internal mobility of the catalytic loops is significantly reduced upon the formation of the ternary complex, but some mobility remains. Some degrees of mobility in the catalytic loops of the ternary complex may be required for the optimal stabilization of the transition state, which may need the instantaneous adjustment and alignment of the side-chain positions of catalytic residues. Such dynamic behaviors may be characteristic of bisubstrate enzymes.

## MATERIALS AND METHODS

*Sample Preparation.* The overexpression and protein purification protocol was similar to that previously described (*13*). Briefly, BL21(DE3) *E. coli* cells containing pET17b-HPPK were grown in LB media. When $OD_{600}$ reached 1.0, the cells were collected and resuspended in M9 media containing $^{15}NH_4Cl$ and [$^{13}C_6$]-D-glucose as the sole nitrogen and carbon sources, respectively, when necessary (*25*). Induction by 100 mg/L IPTG was started 1 h later and lasted 4 h. The cells were then harvested by centrifugation (6000 rpm, 20 min), washed with 20 mL of buffer A (20 mM Tris-HCl, pH 8.0), and kept at −80 °C until use. The frozen bacterial paste was thawed at 42 °C and then sonicated on ice. Following the initial purification by ion-exchange chromatography, fractions containing HPPK were concentrated to ~3 mL by an Amicon concentrator and then applied to a gel filtration column (Sephadex G-75) equilibrated with buffer B (20 mM sodium phosphate, pH 7.4). The column was developed with the same buffer. The purified HPPK fractions were lyophilized. NMR samples were prepared by dissolving the required amount of protein powder in buffer B made with 5% $D_2O$/95% $H_2O$. Great care was taken to

adjust and to keep the pH at 7.4 during NMR experiments. Five $^{15}$N-labeled apo-HPPK samples were prepared with the protein concentrations at 0.1, 0.25, 0.5, 1.0, and 2.0 mM. One $^{15}$N/$^{13}$C-labeled apo-HPPK sample was prepared with the protein concentration at ~0.5 mM for sequential resonance assignment. Two samples of the binary complex of $^{15}$N-labeled HPPK and MgAMPCPP were prepared, one containing 0.5 mM HPPK, 5 mM AMPCPP, and 20 mM $MgCl_2$ and the other containing 1.0 mM HPPK, 10 mM AMPCPP, and 40 mM $MgCl_2$. The dissociation constant of the HPPK·MgAMPCPP complex ($K_d$ of 77 nM) suggests that, under this condition, the protein is saturated with MgAMPCPP (*18*). The ternary complex of HPPK was prepared using AMPCPP, 7,7-dimethyl-6-hydroxypterin (DMHP, an HP analogue), $^{15}$N-labeled HPPK, and $Mg^{2+}$ as previously described (*24*). The NMR sample contained 0.5 mM HPPK, 5 mM AMPCPP, ~2 mM DMHP, and 20 mM $MgCl_2$.

*Sequential Resonance Assignments.* The backbone NMR assignment of the HPPK protein was previously done in the apo state (*12*) and in complex with MgAMPCPP (*24*). The backbone resonance assignment of the apo-HPPK was further extended at a lower concentration of protein (0.5 mM). HNCA and CBCA(CO)NH experiments (*26*) were acquired for the $^{15}$N/$^{13}$C-labeled apo-HPPK sample on a Bruker Avance 800 MHz and a Bruker Avance 500 MHz spectrometer equipped with a cryoprobe. The NMR data were processed with NMRPipe (*27*) and analyzed with NMRView (*28*).

*$^{15}$N Relaxation Measurements.* $^{15}$N relaxation experiments were carried out at 25 °C on a Bruker Avance 600 MHz spectrometer for the apo-HPPK and the binary complex HPPK·MgAMPCPP and on a Varian INOVA 600 MHz spectrometer for the ternary complex HPPK·MgAMPCPP·DMHP. Standard pulse sequences were used to obtain the longitudinal and transverse relaxation rates $R_1$ and $R_2$, as well as $\{^1H\}-^{15}N$ heteronuclear NOEs (*29*). The decays of the $^{15}$N longitudinal and transverse magnetizations for the apo-HPPK and the binary complex were sampled by typically 9 (10, 100, 300, 500, 800, 1200, 1500, and 2000 ms in random order) and 10 points (6, 14, 42, 62, 70, 82, 102, 122, 142, and 162 ms in random order), respectively. The first points of both experiments were duplicated at the end of the experiments to verify the stability of the sample and to estimate the intensity error. The time points were 11, 44, 167, 389, 666, 944, 110, 1443, and 1998 ms for the $R_1$ measurement of the ternary complex and were 17, 35, 52, 70, 87, 104, 122, and 139 ms for the $R_2$ measurement of the ternary complex. The third points of both experiments were repeated for error estimation. The delay $\tau_{cp}$ between $^{15}$N inversion pulses in the CPMG module in $R_2$ experiments was set to 1 ms. A recycle delay of 2.5 s was used for both $R_1$ and $R_2$ experiments. The residue-specific $\{^1H\}-^{15}N$ heteronuclear NOE was measured by dividing the peak intensity in two 2D spectra recorded with and without a 3 s proton presaturation achieved by 120° $^1$H pulses following a 5 s delay (*30*). The experiments were duplicated at each protein concentration to estimate the uncertainty. All of the 2D spectra were recorded with 1024 complex data points and 128 complex increments for the apo-HPPK and the binary complex and with 1994 complex data points and 100 complex increments for the ternary complex. The number of transients was 16 for all relaxation experiments except the $\{^1H\}-^{15}N$ heteronuclear NOE experiment of the ternary complex, which was 64. The spectral widths were set to 8389 and 1460 Hz for the apo-HPPK, 8389 and 1581 Hz for the binary complex, and 9000 and 1720 Hz for the ternary complex in the direct $^1$H and the indirect $^{15}$N dimensions, respectively.

The relaxation data were processed with NMRPipe (*27*) and analyzed with NMRView (*28*). For the relaxation data of the apo-HPPK, a Lorenz-to-Gauss window function was applied in both dimensions, and for those of the binary complex, a cosine-bell window function was applied. A forward-and-backward linear prediction and zero filling were typically used to extend the indirect dimension by a factor of 2. The peak intensities of the relaxation rate measurements were extracted using the NvRatePrintHeight subroutine of NMRView (*28*). Intensities below the noise level were typically removed, and the exponential decay curves were fitted to a two-parameter exponential equation using an in-house modified version of RELAXFIT (*31*). The uncertainties on the relaxation rates were estimated by 500 Monte Carlo simulations. The HetNOE subroutine of NMRView was used to calculate the heteronuclear NOEs. The final values were extracted from the duplicates.

*Rotational Diffusion and Model-Free Analysis.* Rotation diffusion was analyzed using the $R_2/R_1$ values of well-ordered regions of the structure deemed free of either fast internal motion or chemical exchange. Hydrogen atoms were added to the crystal structure (PDB code 1HKA) of the apo-HPPK (*10*) by using MOLMOL (*32*). The mean structures of the NMR ensembles of the binary complex HPPK·MgAMPCPP (PDB code 2F65) (*24*) and the ternary complex HPPK·MgAMPCPP·DMHP (PDB code 2F63) (*24*) were taken as the representative structures of the complexes. The optimization of the rotational diffusion tensor against the experimental data was achieved by using ROTFIT (*33*) and TENSOR2 (*34*). HYDRONMR (*35*) was used to predict the rotational diffusion tensors of the three forms of HPPK based on their structures.

The microdynamic parameters under the Lipari−Szabo formalism (*36*−*38*) were extracted using the TENSOR2 program (*34*). Briefly, the $^{15}$N relaxation data were interpreted in terms of motion of the N−H bond. Five models of increasing complexity were tested including model 1 ($S^2$), model 2 ($S^2$, $\tau_e$), model 3 ($S^2$, $R_{ex}$), model 4 ($S^2$, $\tau_e$, $R_{ex}$), and model 5 ($S^2$, $\tau_e$, $S^2_f$), where $S^2$ is the squared order parameter, $\tau_e$ is a correlation time describing the internal motion (picosecond to nanosecond time scale), assumed to be independent of the overall tumbling, $S^2_f$ is a second squared order parameter describing the fast internal motion on the picosecond to nanosecond time scale, and $R_{ex}$ is the chemical exchange contribution to $R_2$. The *F*-test statistics was then used to select the model that satisfies the data with the lower number of parameters. Standard errors in the model-free parameters were evaluated by 100 Monte Carlo simulations.

## RESULTS

*Extension of Backbone Resonance Assignments of the Apo-HPPK.* HPPK consists of 158 amino acid residues, 12 of which are prolines. The sequential resonance assignment of the apo-HPPK has been previously achieved at 1.5 mM

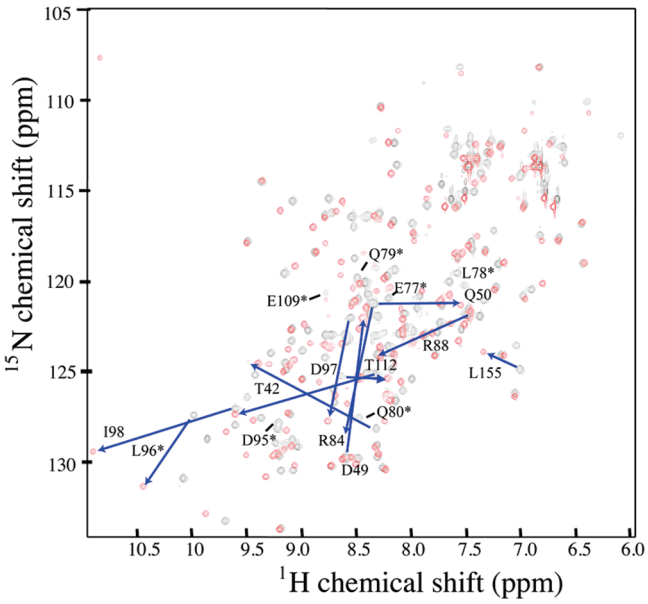


FIGURE 2: The $^{1}$H−$^{15}$N-HSQC spectrum of HPPK in the apo state (black) and in complex with MgAMPCPP (red). The spectra were acquired on a Bruker 600 MHz spectrometer at 25 °C and 0.5 mM protein concentration. The most shifted cross-peaks upon MgAMPCPP complexation are labeled according to their corresponding residue number in the sequence, and the arrow joins the cross-peaks in apo and bound states. In addition, newly assigned cross-peaks of the apo-HPPK are labeled with a star.

protein concentration (*12*). Several residues could not be assigned due to missing $^{1}$H/$^{15}$N cross-peaks in the $^{15}$N-HSQC spectra of apo-HPPK under these conditions. Additional $^{15}$N-HSQC spectra were collected at lower concentrations (0.1, 0.25, 0.5, 1 mM). Overall, the $^{15}$N-HSQC cross-peaks were sharpened with decreasing the protein concentration. Several additional cross-peaks could be observed at 0.5 mM that were absent at 1 mM concentration, and concomitantly, 10 cross-peaks showed small chemical shift variations ($|\Delta_{^{1}H}|_{max} < 0.04$ ppm and $|\Delta_{^{15}N}|_{max} < 0.5$ ppm). Below 0.5 mM protein concentration, the spectra were exactly superimposable. Two triple resonance experiments (HNCA and CBCACONH) were acquired on a 0.5 mM $^{13}$C/$^{15}$N-labeled apo-HPPK sample to extend the backbone resonance assignment. Seven additional residues could be assigned (Figure 2): E77, L78, Q79, and Q80 in the C-terminal extremity of helix α2, D95 and L96 in strand $\beta$4, and E109 at the turn of the $\beta$-hairpin $\beta$5−$\beta$6. About 10 weak $^{1}$H−$^{15}$N correlation peaks in the $^{15}$N HSQC could not be unambiguously assigned. They likely correspond to residues Q48 in loop 2, R82, V83, A86, W89, G90, R92, and T93 in loop 3, and Y116 between strand $\beta$6 and helix α3, which remain unassigned.

*$^{15}$N Relaxation Data and Indications of Weak Self-Association of the Apo-HPPK.* Initial NMR studies indicated that the $^{15}$N relaxation parameters of the apo-HPPK were protein concentration dependent, which is usually indicative of self-association. To ascertain the effects of the self-association on the relaxation parameters, we collected the residue-specific $^{15}$N $R_1$, $R_2$, and {$^{1}$H}−$^{15}$N heteronuclear NOE data of apo-HPPK at four protein concentrations: 0.1, 0.5, 1, and 2 mM. Because of peak overlaps, unassigned residues, and weak signals leading to decay curves of poor quality, $^{15}$N relaxation data could be obtained for 118, 118, 112, and 104 residues out of the 146 nonproline residues for 0.1, 0.5, 1, and 2 mM samples, respectively. Fewer data were obtained at high concentrations, because of line broadening and peak disappearance. Figure 3 shows the distribution of these data as well as the $R_2/R_1$ ratio versus the amino acid sequence at the four concentrations. The mean $R_1$ values were 1.12 ± 0.06, 1.14 ± 0.06, 1.06 ± 0.05, and 0.76 ± 0.06 s$^{-1}$ at 0.1, 0.5, 1, and 2 mM, respectively, and the corresponding mean $R_2$ values were 13.15 ± 1.82, 14.32 ± 2.38, 16.24 ± 2.90, and 26.30 ± 4.21 s$^{-1}$. The mean $R_1$ value decreased significantly whereas the mean $R_2$ value increased significantly at 1 and 2 mM HPPK compared with the values at 0.1 and 0.5 mM, suggesting a significant self-association at higher concentrations.

On the individual residue basis, all of the secondary structure elements had $R_1$, $R_2$, and NOE values near the mean values at each concentration, except the C-terminal extremity of the helix α2 (residues R75−Q80) and the N-terminal extremity of the strand $\beta$4 (residues L94 and D97), both of which are linked to loop 3 and had higher $R_2$ values. Loop 1 also contained higher than averaged $R_2$ values. In contrast, residues in loops 2 and 3 have a lower than averaged $R_2$ together with low NOE values. The NOE values at different concentrations were quite similar, except some variations in loops 1, 2, and 3, indicating that protein concentration does not have significant effects on the internal motions of the protein on the picosecond to nanosecond time scale.

The averaged $R_2/R_1$ values were used to obtain the estimate of the isotropic correlation times ($\tau_c$) of the protein. At 0.1 mM, the uncertainties in the relaxation data were relatively high so that the isotropic diffusion model ($\tau_c$ = 10.48 ± 0.25 ns) was statistically sufficient to describe the rotational diffusion properties of HPPK. At 0.5, 1, and 2 mM concentrations, the rotational diffusion of HPPK was estimated to be fully anisotropic. The ratios of the estimated principal components were quite similar at each concentration (1:0.83:0.76, 1:0.79:0.73, and 1:0.81:0.75, at 0.5, 1, and 2 mM, respectively), and the corresponding $\tau_c$ values were 10.87 ± 0.31, 12.28 ± 0.42, and 19.30 ± 0.71 ns. The rotational diffusion tensors at 0.1 and 0.5 mM concentrations were in excellent agreement with that predicted by HYDRONMR (*35*) on the crystal structure of the monomeric form of the apo-HPPK (PDB code 1HKA, ratios of the principal components of 1:0.80:0.70 and averaged correlation time of 10.22 ns). The significant increases in $\tau_c$ at 1 and 2 mM are likely due to the self-association of HPPK at high concentrations.

The changes of $^{1}$H and $^{15}$N chemical shifts and peak intensity in the $^{15}$N-HSQC spectra of HPPK were also monitored at five concentrations: 0.1, 0.25, 0.5, 1, and 2 mM. The chemical shift changes were not significant in the 0.1−0.5 mM concentration range whereas the chemical shifts of quite a few residues were found to vary at protein concentrations higher than 1 mM. The changes were relatively small for most of these residues, however. Attempts were made to determine the $K_d$ value for the self-association from the cross-peaks with the largest chemical shift changes. However, as the $^{1}$H and $^{15}$N chemical shifts changed in a linear fashion with the protein concentration (Supporting Information Figure S1), it was not possible to estimate the $K_d$ value for the self-association. These results nevertheless indicated that the self-association of HPPK is weak in the studied concentration range.

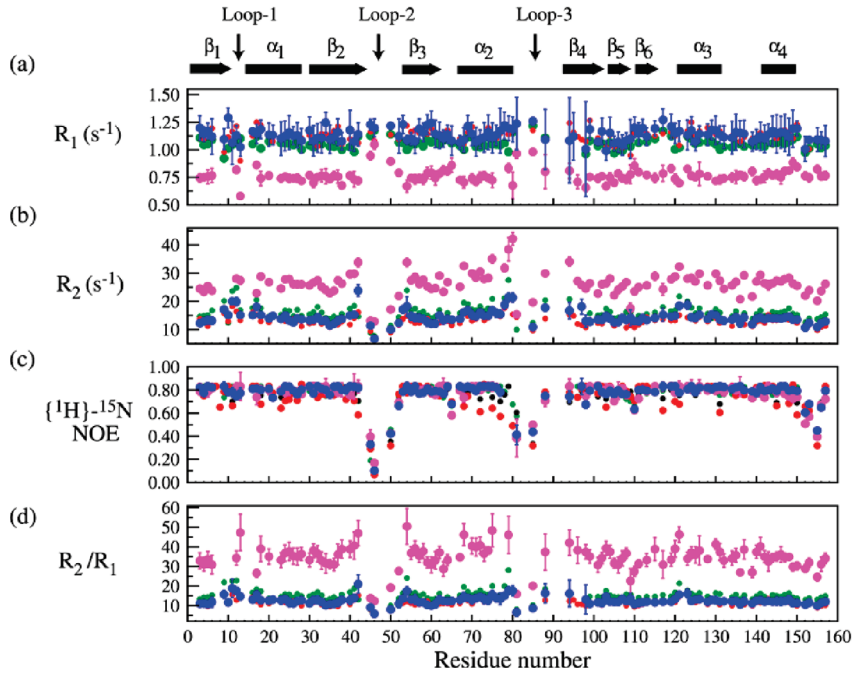


FIGURE 3: $^{15}$N relaxation parameters obtained for the apo-HPPK at 25 °C at four concentrations: 0.1 mM (red), 0.5 mM (blue), 1 mM (green), and 2 mM (magenta). For matter of clarity, the estimated uncertainties are not represented at 0.1 and 1 mM concentrations. The secondary structure of the apoprotein is represented at the top of the figure. (a) $R_1$ relaxation rates; (b) $R_2$ relaxation rates; (c) $\{^1H\}-^{15}N$ NOE values; and (d) $R_2/R_1$ ratio.

Taken together, the results of the relaxation, rotational diffusion tensors, and chemical shift analysis over the four studied samples suggested that the apo-HPPK is prone to self-associate in the millimolar range concentration. However, the self-association of the apo-HPPK is insignificant at 0.1 and 0.5 mM protein concentrations.

*$^{15}$N Relaxation Data Analysis of the Binary Complex HPPK·MgAMPCPP.* MgAMPCPP was used as an analogue for the substrate MgATP, as HPPK had a low level of ATPase activity. MgAMPCPP is an excellent MgATP analogue for HPPK with respect to both structure (*14*) and binding affinity (*18*). Binding of MgAMPCPP caused significant changes in the $^{15}$N-HSQC spectrum (Figure 2). All expected backbone resonances were previously assigned at 1.6 mM protein concentration, except those of residues T1, S13, E16, R82, W89, G90, and L94, which were missing (*24*). Several residues in loops 2 and 3 showed two or more sets of cross-peaks, including L45-Q50 in loop 2 and A86-E87 in loop 3 (*24*). Additional $^{15}$N-HSQC spectra were acquired at both 0.5 and 1 mM concentrations of the HPPK·MgAMPCPP complex. No significant change in chemical shifts was observed. For the relaxation study, we extracted the relaxation data for the most populated isomer. $^{15}$N $R_1$, $R_2$, and $\{^1H\}-^{15}N$ heteronuclear NOEs were measured for 130 and 129 residues at the 0.5 and 1 mM concentrations of the complex, respectively. The results are shown in Figure 4. At 0.5 mM, the mean $R_1$ and $R_2$ were 1.29 ± 0.20 and 12.64 ± 3.50 s$^{-1}$, respectively, and the corresponding values at 1 mM were 1.16 ± 0.10 and 14.83 ± 4.60 s$^{-1}$. Similar to the apoprotein, a small increase in $R_2$ was accompanied by a decrease in $R_1$, suggesting that the binding of MgAMPCPP does not completely prevent the weak self-association of HPPK, as the derived $\tau_c$ values slightly increased between 0.5 mM (9.26 ± 0.30 ns) and 1 mM (10.25 ± 0.20 ns) concentrations. However, these $\tau_c$ values were shorter than the $\tau_c$ value predicted by HYDRONMR (10.42 ns) on the basis of the mean structure of the HPPK·MgAMPCPP complex, suggesting that the monomeric form of the complex is highly predominant at both concentrations. The $R_2/R_1$-derived anisotropic rotational diffusion model at 0.5 mM complex concentration had ratios of the principal components of 1:0.95:0.78, similar to those predicted based on the mean NMR structure of the HPPK·MgAMPCPP complex (1:0.89:0.81). Taken together, both the chemical shift and the rotational diffusion tensor data indicated that the self-association of HPPK is weakened upon the binding of MgAMPCPP and that the self-association can be regarded as insignificant for the HPPK·MgAMPCPP complex at 0.5 mM concentration.

*$^{15}$N Relaxation Data Analysis of the Ternary Complex HPPK·MgAMPCPP·DMHP.* Except the first residue, sequential resonance assignment has been made for all residues, including those from the three catalytic loop region (*24*). $^{15}$N relaxation data could be obtained for 135 residues (Figure 5), 5 more residues than the binary complex. The mean $R_1$ and $R_2$ were 1.32 ± 0.06 and 11.51 ± 0.94 s$^{-1}$, respectively. While the mean $R_1$ was similar to that of the binary complex, the mean $R_2$ of the ternary complex was significantly smaller, with a much smaller standard deviation as well. The uniformity of the $R_2$ values was consistent with the uniformity of the intensities of the $^1H-^{15}N$-HSQC cross-peaks of the ternary complex, indicating that the protein is rigidified upon the formation of the ternary complex. The $\tau_c$ value of the ternary complex was estimated to be 8.88 ± 0.01 ns based on the averaged $R_2/R_1$ ratio, shorter than the $\tau_c$ value predicted by HYDRONMR (10.42 ns) based on the mean structure of the ternary complex. The $R_2$ data and the correlation times indicated that the ternary complex has a more compact structure than the apo-HPPK and the binary complex. The ratios of the estimated principle components were 1:0.87:0.89, similar to those calculated using the mean NMR structure of the ternary complex (1:0.86:0.92).

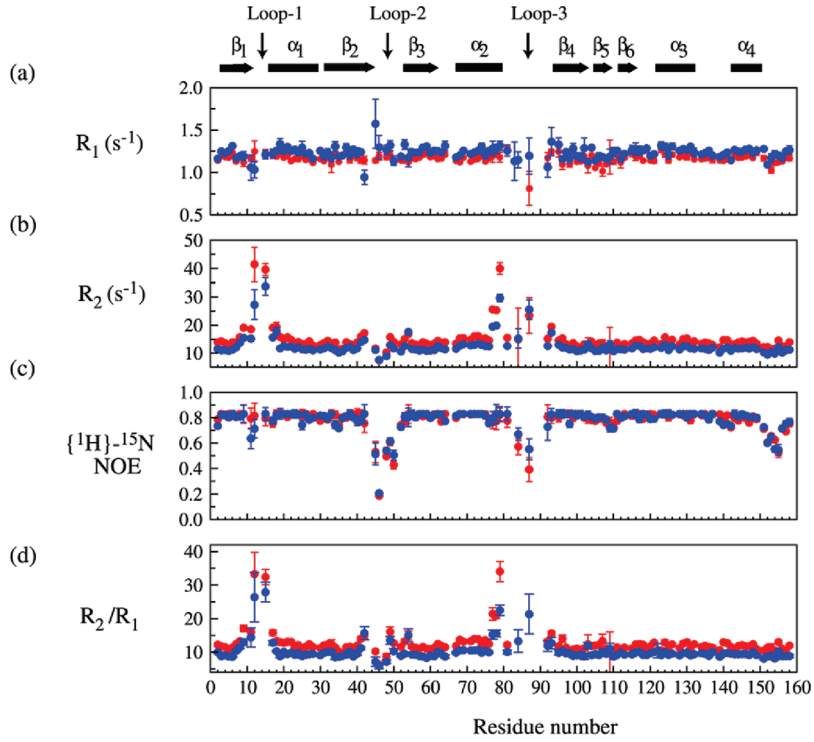


FIGURE 4: $^{15}$N relaxation parameters obtained for the binary complex HPPK·MgAMPCPP at 25 °C at two concentrations: 0.5 mM (blue) and 1 mM (red). The secondary structure is represented at the top of the figure. (a) $R_1$ relaxation rates; (b) $R_2$ relaxation rates; (c) {$^1$H}−$^{15}$N NOE values; and (d) $R_2/R_1$ ratio.

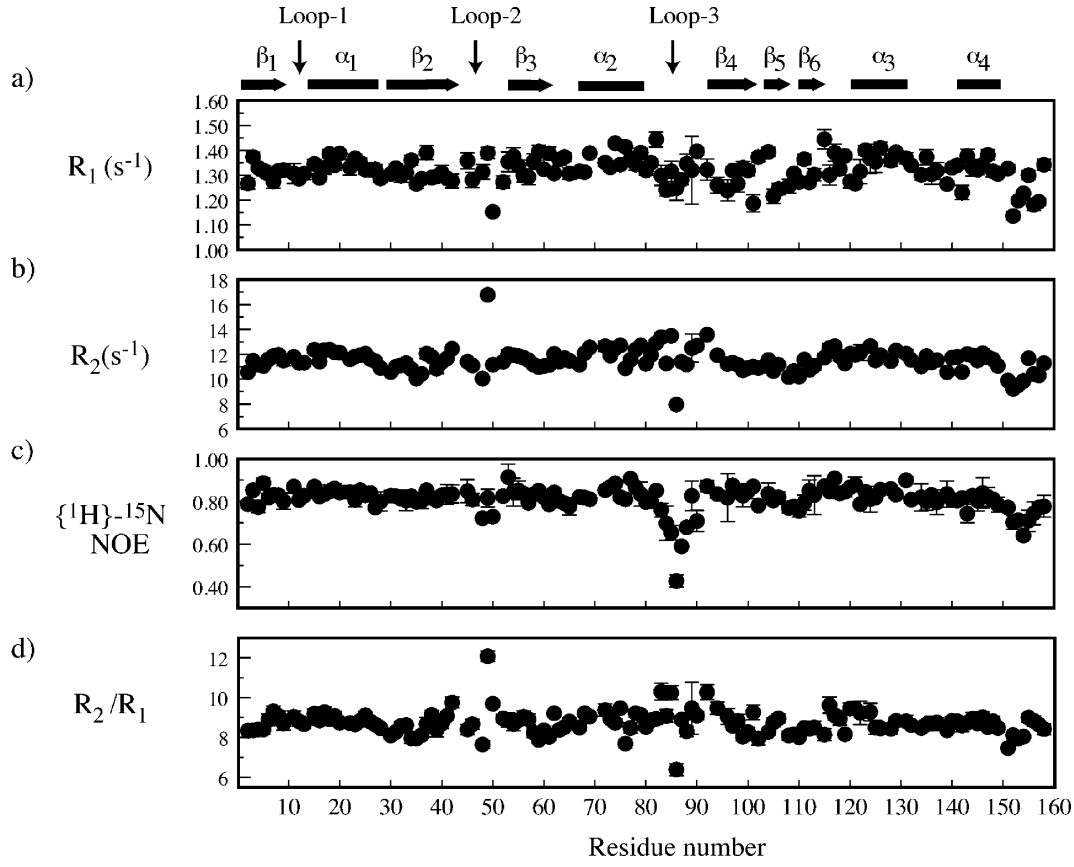


FIGURE 5: $^{15}$N relaxation parameters obtained for the ternary complex HPPK·MgAMPCPP·DMHP at 25 °C. The secondary structure is represented at the top of the figure. (a) $R_1$ relaxation rates; (b) $R_2$ relaxation rates; (c) {$^1$H}−$^{15}$N NOE values; and (d) $R_2/R_1$ ratio.

*Model-Free Analysis of the Three Forms of HPPK.* The microdynamic parameters of the apo-HPPK were extracted in the model-free framework (*36*−*38*). HPPK is in rather low abundance *in vivo* and therefore most likely functions in a monomeric form (*39*−*41*). Therefore, our analysis was performed on the relaxation data obtained at 0.5 mM protein concentration, because the data acquired at this concentration had excellent quality and the self-association of the protein

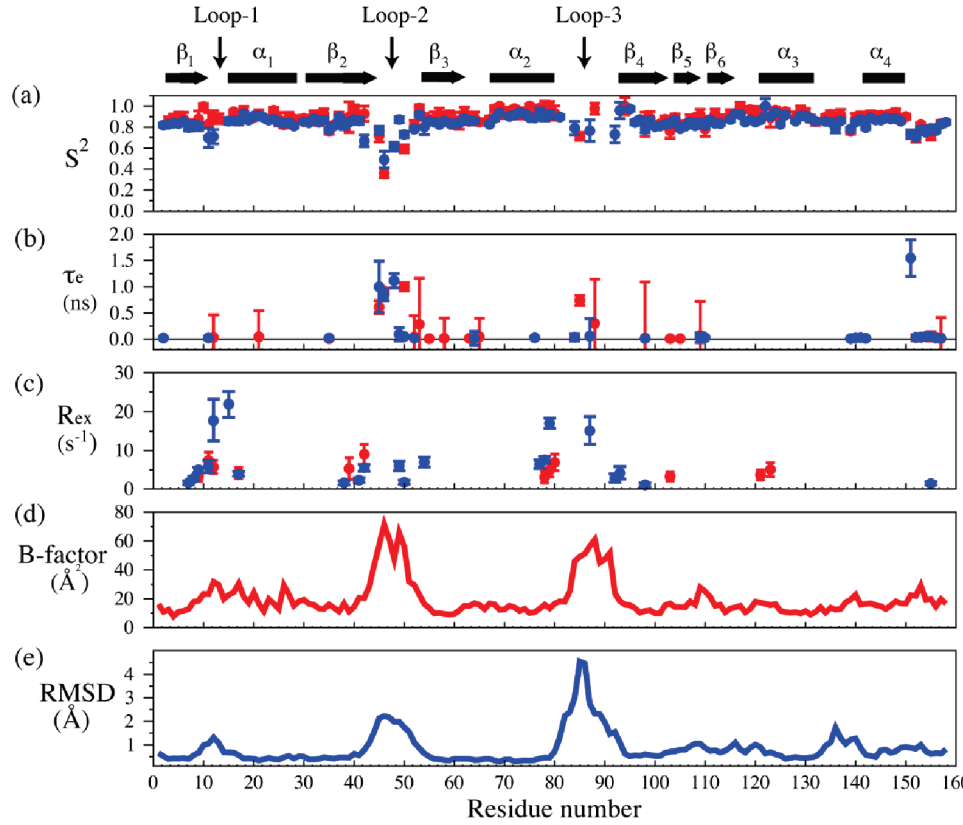


FIGURE 6: Comparison of the model-free parameters versus residue number between the apo-HPPK (red) and the binary complex with MgAMPCPP (blue) at 0.5 mM protein concentration. The secondary structure is represented at the top of the figure. (a) Squared order parameter $S^2$; (b) correlation time ($\tau_e$) of internal motion; (c) chemical exchange contribution $R_{ex}$; (d) $C_\alpha$ atom *B*-factors of the crystal structure of the apo-HPPK (in red); and (e) backbone rms deviations of the NMR structure of the binary complex with MgAMPCPP (in blue).

was insignificant. The model-free parameters $S^2$, $\tau_e$, and $R_{ex}$ could be extracted for 118 residues and are presented in Figures 6 and 8. The mean $S^2$ was 0.88 ± 0.08. All residues in the secondary structure, except T35 in the distorted strand $\beta$2, had $S^2$ values higher than 0.8, indicating that the secondary structure elements are rigid. The four helices were slightly more rigid than the central $\beta$-sheet with mean $S^2$ values of 0.92 and 0.86, respectively. In addition to T35, the following residues had significantly lower $S^2$ values than the mean: L45, G46, Q50, R85, N103, V105, R110, F139, F152, L155, and N156. Residues L45, G46, and Q50 are located in loop 2 (Figure 1); R85 is located in loop 3; N103, V105, R110, and D139 are located in short turns; and F152, L155, and N156 are in the C-terminal region. Twelve residues required the introduction of a significant $R_{ex}$ term (higher than 2 $s^{-1}$) for the model-free analysis: S9, L11, A12, Q17, F39, T42, L78-Q80, N103, R121, and F123. Residues S9, L11, and A12 are located in loop 1; Q17 is located in the N-terminal region of helix α2 connected to loop 1; F39 is in the C-terminal region of the distorted strand $\beta$2 connected to loop 2; T42 is in loop 2; L78−Q80 are in the C-terminal region of helix α2 connected to loop 3; R121 is in the loop connected to helix α3; and F123 is in the N-terminal region of helix α3.

The microdynamic parameters of the binary complex HPPK·MgAMPCPP are also summarized in Figures 6, 7, and 8 for comparison with those of both the apo-HPPK and the ternary complex. The mean $S^2$ was 0.84 ± 0.07, similar to that of the apo-HPPK. Significant chemical exchange (higher than 1.5 $s^{-1}$) was introduced for 17 residues: G8, S9, L11, A12, L15, and Q17 around loop 1, T42, D49, and L54 around loop 2, E77, L78, Q79, E87, R92, T93, and L96 around loop 3, and N103 in loop $\beta$4−$\beta$5. The dynamic properties of the HPPK·MgAMPCPP complex are similar to those of the apoenzyme with some regions becoming even more mobile upon the binding of the nucleotide.

The microdynamic parameters of the ternary complex HPPK·MgAMPCPP·DMHP are summarized in Figures 7 and 8. The mean value for $S^2$ was 0.88 ± 0.04, similar to those of the apo-HPPK and the binary complex. However, only five residues were below two standard deviations of the mean value: Q48, A86, A151, F152, and D153. Q48 and A86 are located in loops 2 and 3, respectively, and residues 151−153 in the C-terminal region. Only four residues required a significant $R_{ex}$ term (higher than 1.5 Hz) for the model-free analysis: D49, V83, K85, and R92; the $R_{ex}$ values were significantly smaller than those of the binary complex. Residue 49 is located in loop 2 and residues 83, 85, and 92 are located in loop 3. The results indicated that the C-terminal region is mobile as in the apo-HPPK and the binary complex; the catalytic loops are significantly rigidified upon the formation of the ternary complex. However, loops 2 and 3 retain some degrees of mobility.

In general, several physical phenomena are prone to give rise to chemical exchange. In the case of HPPK, self-association represents a potential source of chemical exchange. Although the results from model-free analysis are known to be affected when self-association is severe (*42*), we estimated the chemical exchange $R_{ex}$ from the data obtained on HPPK in the apo form at all concentrations (data

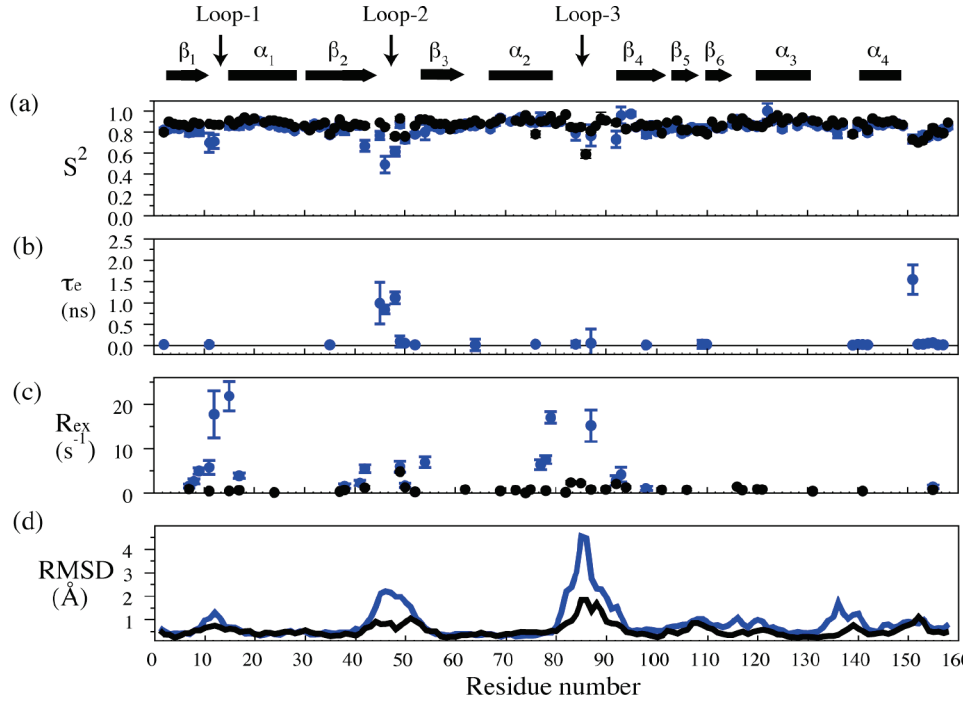


FIGURE 7: Comparison of the model-free parameters versus residue number between the binary complex HPPK·MgAMPCPP (blue) and the ternary complex HPPK·MgAMPCPP·DMHP (black) at 0.5 mM protein concentration. The secondary structure is represented at the top of the figure. (a) Squared order parameter $S^2$; (b) correlation time ($\tau_e$) of internal motion; (c) chemical exchange contribution $R_{ex}$; and (d) backbone rms deviations.

not shown). We did not observe any significant systematic trend in $R_{ex}$ over the four concentrations that could be associated with self-association (as discussed in ref *43*). As a consequence, the contribution of self-association to the chemical exchange was judged to be insignificant. In addition, the fast exchange between the apo and the bound states of the protein can also induce chemical exchange, if the chemical shifts of a given spin differ significantly in the two states. In such a situation, the chemical exchange can be estimated to be proportional to the product of the two populations in exchange (*44*). Given the dissociation constant of the binary complex (77 nM) (*18*) and the high concentration of AMPCPP, the contribution of the dissociation of the binary complex to the chemical exchange was judged to be insignificant. Taken together, we concluded that the chemical exchanges observed in both the apo and the nucleotide-bound states were mainly associated with the intrinsic internal mobility of the monomeric forms of the apo-HPPK and of the binary complex.

## DISCUSSION

HPPK undergoes dramatic conformational changes during its catalytic cycle, and the conformational changes play important roles in HPPK catalysis (Figure 1b) (*10*−*12, 14, 16, 21*−*24*). In order to fully understand the roles of conformational dynamics in HPPK catalysis, we carried out the first direct experimental measurement of backbone dynamics of HPPK by NMR, focusing on the formation of the Michaelis complex. Our analysis was, however, complicated by the weak self-association of HPPK at high concentrations. Therefore, we made $^{15}N$ relaxation measurements at four protein concentrations for the apo-HPPK and at two concentrations for the binary complex HPPK·MgAMPCPP. Based on the chemical shifts, relaxation parameters, and correlation time analysis, we concluded that self-association is insignificant for the apo-HPPK and for the binary complex HPPK·MgAMPCPP at 0.5 mM protein concentration. Therefore, we focused our analysis on the relaxation data acquired at this concentration on both states of HPPK using the model-free formalism (*36*−*38*).

In the model-free framework, the squared order parameter $S^2$ reflects the amplitude of internal motions on the picosecond to nanosecond time scale, the internal correlation time $\tau_e$ gives an estimation of the time scale for these motions, and $R_{ex}$ reflects conformational exchange on the microsecond to millisecond time scale. Overall, the core structure of the enzyme remains highly rigid on the picosecond to nanosecond and microsecond to millisecond time scales in all three forms. This region includes one-half of the cleft forming the active site, which contains the residues in strands $\beta$4, $\beta$5, and $\beta$6 that are in contact with the nucleotide, and was previously referred as the rigid wall (*10*). This observation is consistent with the published structures, which indicate that the core structure of HPPK region is mostly structurally invariant (with very small backbone rms deviations) with respect to ligand binding or mutations (*10*−*12, 14, 16, 21*−*24*). We also notice that the C-terminal region of the protein is flexible on the picosecond to nanosecond time scale in all three forms, in consistence with elevated rms deviations of this region when the structures of the various forms of the wild-type and mutant HPPKs are superimposed. Since the C-terminal extremity is in contact with strand $\beta$2, near the HP substrate binding site, mobility in this region may be required for the fine adjustment of the local conformation of the HP-binding site during the catalytic reaction. Because the major conformational changes during the catalytic cycle are localized in the three catalytic loops, we will focus our

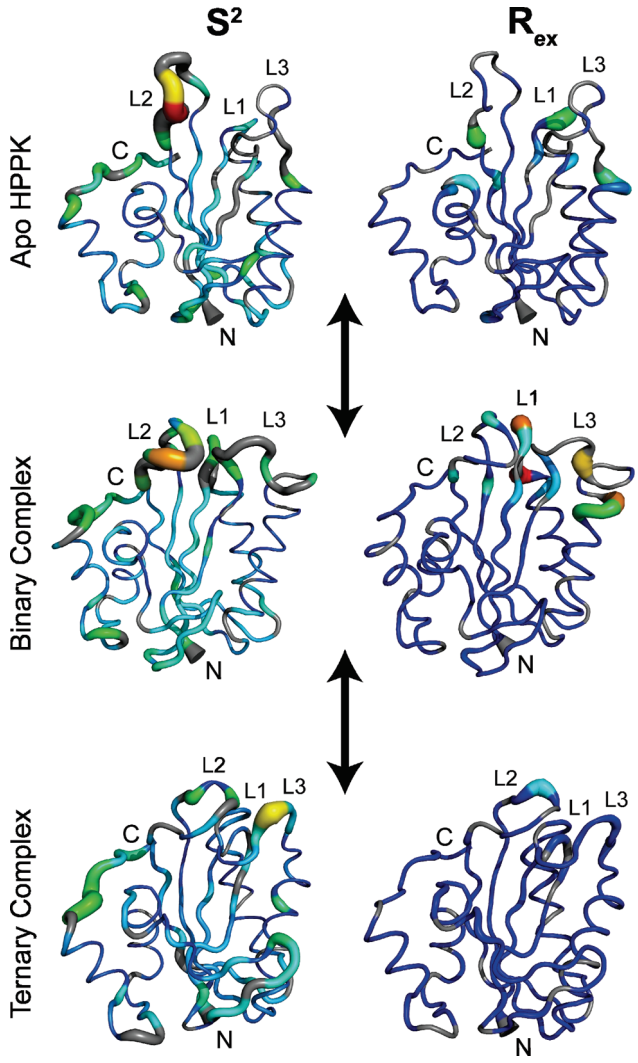


FIGURE 8: Mapping of the dynamic parameters $S^2$ (left panel) and $R_{ex}$ (right panel) to the structures of the apo-HPPK (top), the binary complex (HPPK·MgAMPCPP, middle), and the ternary complex (HPPK·MgAMPCPP·DMHP, bottom). The $S^2$ values are scaled by a color gradient with the smallest value in red and the largest value in blue. The $R_{ex}$ values are scaled by a color gradient with the smallest value in cyan and the largest value in red, and residues without an $R_{ex}$ term are colored in blue. Residues without the measured dynamic parameters, i.e., 12 proline residues and other residues with missing or overlapping NH cross-peaks, are in gray. The figure was made with PyMOL (*45*).

discussion on the dynamic properties of these loops and their changes in the conformational transitions from the apo-HPPK to binary substrate complex to the Michaelis complex.

Based on the $S^2$ values, loop 1 of the apo-HPPK is rigid on the picosecond to nanosecond time scale (Figures 6a and 8). Its mean $S^2$ value is $0.90 \pm 0.06$, comparable to those of the four helices and the central $\beta$-sheet, which have mean $S^2$ values of 0.92 and 0.86, respectively. On the other hand, the model-free analysis of the relaxation data introduced a chemical exchange term for three residues of this short loop (S9, L11, and A12) (Figures 6c and 8), suggesting that loop 1 undergoes conformational exchange on the microsecond to millisecond time scale. The crystal structure of the apo-HPPK reveals two conformations for this loop with moderate *B*-factor values (Figure 1b) (*10*). The dynamic properties of loop 1 determined in this NMR work therefore suggest that the two conformations are likely in exchange on the microsecond to millisecond time scale. Upon the binding of the nucleotide, loop 1 undergoes conformational exchange on the microsecond to millisecond time scale to a similar extent to that of the apo-HPPK. Nevertheless, loop 1 becomes significantly more mobile on the picosecond to nanosecond time scale. Indeed, the mean $S^2$ value of the loop is 0.71 for the binary complex and 0.90 for the apo-HPPK.

The model-free parameters indicate that loop 2 is significantly mobile on the picosecond to nanosecond time scale in the apo-HPPK, with a mean $S^2$ value of $0.62 \pm 0.20$ (Figure 6a and 8). Due to the presence of four proline residues (P43, P44, P47, and P51), missing or overlapping cross-peaks, the dynamic properties of only four residues of loop 2 (P43-D52) were accessible. The $S^2$ values of L45, G46, and Q50 are 0.72, 0.36, and 0.59, respectively, and that of D52 (0.82) is close to the average $S^2$ value of the enzyme (0.88). The $S^2$ values of the loop residues vary greatly with the middle region (around G46) having the lowest $S^2$ values. It is also noticed that the two residues that delimit the loop are rigid on the picosecond to nanosecond time scale with $S^2$ values of 0.93 and 0.98 for T42 and Q53, respectively. Surprisingly, although two residues (F39 and T42) in the twisted strand $\beta$2 that precedes loop 2 required an $R_{ex}$ term for the model-free analysis, none of the loop 2 residues required an $R_{ex}$ term (Figure 6c and 8), suggesting that loop 2 does not undergo significant conformational exchange on the microsecond to millisecond time scale.

Upon the binding of MgAMPCPP, loop 2 remains highly flexible on the picosecond to nanosecond time scale with an only minor increase in $S^2$ compared with the apoprotein. In contrast to the apo-HPPK, mobility on slow time scales (slower than the microsecond time scale) could be observed in loop 2 in the complex. Indeed, significant chemical exchange was detected in loop 2 (for residue D49, $R_{ex}$ of $6.1 \pm 1.5$ $s^{-1}$), and the existence of (at least) two sets of cross-peaks for many consecutive residues in loop 2 (*24*) may suggest that this loop also undergoes conformational isomerization at an even slower exchange rate (at the NMR time scale). Furthermore, the intensity ratios of the major and the minor peaks are significantly different for some residues, suggesting that loop 2 may assume multiple conformations. It is possible that the slow conformational exchanges are due to a *cis*−*trans* isomerization of the four proline residues (P43, P44, P47, and P51), but no NMR indication for a *cis* configuration was observed for any of the four proline residues and all are in a *trans* configuration in the NMR and crystal structures. The mobility of loop 2 in the HPPK·MgAMPCPP complex is consistent with the structures of HPPK in complex with nucleotides. Indeed, the backbone rms deviations of loop 2 in the NMR structure of the HPPK·MgAMPCPP complex are significantly higher than other regions of the protein (*24*) (Figure 6e). The increased mobility of loop 2 is further supported by the loss of electron density for a significant part of the loop (residues 44−48) upon binding of MgADP (*16*).

The dynamic properties could be directly obtained only for two residues in loop 3 for the apo-HPPK. This is mainly due to the weakness or absence of NMR signals for the NH groups of residues R82, V83, A86, W89, G90, and R92, which clearly indicates that loop 3 is flexible and undergoes conformational exchange at an intermediate rate (at the chemical shift time scale). In addition, conformational

exchange occurring on the microsecond to millisecond time scale was detected for several residues at the extremity of helix α2 linked to loop 3 (Figure 8). Similar to the apo-HPPK, the weak intensity of most cross-peaks corresponding to residues in loop 3 precluded the accurate measurements of the relaxation parameters in loop 3 in the HPPK·MgAMPCPP complex. This indicates that loop 3 remains highly mobile on the intermediate time scale upon the binding of the nucleotide. The existence of internal mobility of loop 3 is also enforced by the presence of chemical exchange on the microsecond to millisecond time scale for residues at the bottom of the loop and for E87 in the middle of the loop (Figures 6c and 8) and by the multiple chemical shifts observed for A86 and E87, suggesting that, like loop 2, loop 3 also undergoes conformational exchange on an even slower time scale.

In summary, the binding of the nucleotide does not quench the internal motions of HPPK on the picosecond to nanosecond, microsecond to millisecond, and millisecond to second time scales, as evidenced by the $S^2$ and $R_{ex}$ values, weak and missing cross-peaks, and multiple cross-peaks with different intensity ratios. The mobilities of the three catalytic loops remain the same or are even enhanced upon the binding of the nucleotide. The result is consistent with the biochemical data indicating that the entropy of binding is in favor of the formation of the HPPK·MgATP complex (*13*). It is also consistent with the structural data revealing that the catalytic loops of the enzyme can assume different conformations upon the binding of a nucleotide (*16, 24*).

The motions of the three catalytic loops are significantly quenched upon the formation of the ternary complex (Figures 7 and 8). Loop 1 is represented by S9, L11, and A12. Although the $S^2$ values of S9 in the binary and the ternary complexes (0.83 and 0.88, respectively) are similar, S9 has a significant $R_{ex}$ term (4.3) in the binary complex but not in the ternary complex. The $S^2$ values of L11 and A12 increase significantly from the binary complex (0.71 and 0.72, respectively) to the ternary complex (0.88 and 0.87, respectively), and meanwhile, both residues have a significant $R_{ex}$ term (5.5 and 17.6, respectively) in the binary complex but not in the ternary complex. For loop 2, T42, L45, G46, and Q48 have significantly higher $S^2$ values in the ternary complex (0.86, 0.89, 0.85, and 0.76, respectively) than in the binary complex (0.66, 0.77, 0.52, and 0.64, respectively). Other residues have similar $S^2$ values in the two states. Two residues have a significant $R_{ex}$ term (5.6 for T42 and 6.1 for D49) in the binary complex, whereas only one residue (D49) has a significant $R_{ex}$ term (4.8 $s^{-1}$). For loop 3, relaxation data could be obtained for only three out of ten non-proline residues in the binary complex, because of weak or missing cross-peaks, but for all non-proline residues in the ternary complex. Of the three residues measured for both complexes, the $S^2$ value of R92 increases significantly from the binary complex (0.71) to the ternary complex (0.89), whereas those of the other two residues (R84 and E87) are similar between the two complexes. E87 and R92 in the binary complex have $R_{ex}$ values of 14.7 and 3.3 $s^{-1}$, respectively, whereas only R92 has a significant $R_{ex}$ term of 2.0 $s^{-1}$ in the ternary complex.

While the motions of the three catalytic loops are significantly quenched upon the formation of the ternary complex, the two large loops that are directly involved in the binding of the substrates retain some degrees of mobility. The $S^2$ values of Q48 in loop 2 (0.76) and A86 in loop 3 (0.59) are lower than the mean value by more than two standard deviations. Furthermore, D49 in loop 2 and V83, K85, and R92 in loop 3 have a significant $R_{ex}$ term, ranging from 2.0 to 4.8 $s^{-1}$.

The dynamic properties of HPPK may be characteristic of bisubstrate enzymes. The hallmarks of enzymatic catalysis are the formation of enzyme−substrate complexes and the maximization of transition state stabilization, which have conflicting structural requirements. The formation of an enzyme−substrate complex requires an open active center so that the substrate(s) can get in. On the other hand, the maximization of transition state stabilization requires a closed active center that maximizes the favorable interactions between the enzyme and the transition state. The conflicting structural requirements can be resolved by a flexible active center that can sample both open and closed conformational states. For a bisubstrate enzyme like HPPK, the Michaelis complex consists of two substrates in addition to the enzyme. The enzyme must remain flexible upon the binding of the first substrate so that the second substrate can get into the active center. The active center is fully assembled and stabilized only when both substrates bind to the enzyme. However, the side-chain positions of the catalytic residues in the Michaelis complex are still not optimally aligned for the stabilization of the transition state, which lasts only approximately $10^{-13}$ s. The instantaneous and optimal alignment of catalytic groups for the transition state stabilization requires a dynamic enzyme, not an enzyme which undergoes a large scale of movements but an enzyme which permits at least a small scale of adjustment of catalytic group positions. The dynamic properties of the three forms of HPPK as determined by the $^{15}N$ relaxation measurements are consistent with the conformational transitions for a bisubstrate enzyme from the apo form to the binary substrate complex and the ternary Michaelis complex.

## SUPPORTING INFORMATION AVAILABLE

One figure illustrating the protein concentration dependence of the chemical shifts of the backbone amide protons of the apo-HPPK. This material is available free of charge via the Internet at http://pubs.acs.org.

## REFERENCES

1. Bermingham, A., and Derrick, J. P. (2002) The folic acid biosynthesis pathway in bacteria: Evaluation of potential for antibacterial drug discovery. *BioEssays 24*, 637–648.
2. Blakley, R. L., and Benkovic, S. J. (1984) *in Folates and Pterins*, John Wiley & Sons, New York.
3. Benkovic, S. J., and Hammes-Schiffer, S. (2003) A perspective on enzyme catalysis. *Science 301*, 1196–1202.
4. Boehr, D. D., Dyson, H. J., and Wright, P. E. (2006) An NMR perspective on enzyme dynamics. *Chem. Rev. 106*, 3055–3079.
5. Hammes, G. G. (2002) Multiple conformational changes in enzyme catalysis. *Biochemistry 41*, 8221–8228.
6. Hammes-Schiffer, S., and Benkovic, S. J. (2006) Relating protein motion to catalysis. *Annu. Rev. Biochem. 75*, 519–541.
7. Henzler-Wildman, K., and Kern, D. (2007) Dynamic personalities of proteins. *Nature 450*, 964–972.
8. Olsson, M. H. M., Parson, W. W., and Warshel, A. (2006) Dynamical contributions to enzyme catalysis: Critical tests of a popular hypothesis. *Chem. Rev. 106*, 1737–1756.
9. Saen-Oon, S., Ghanem, M., Schramm, V. L., and Schwartz, S. D. (2008) Remote mutations and active site dynamics correlate with

catalytic properties of purine nucleoside phosphorylase. *Biophys. J. 94*, 4078–4088.
10. Xiao, B., Shi, G. B., Chen, X., Yan, H., and Ji, X. (1999) Crystal structure of 6-hydroxymethyl-7,8-dihydropterin pyrophosphokinase, a potential target for the development of novel antimicrobial agents. *Structure 7*, 489–496.
11. Stammers, D. K., Achari, A., Somers, D. O., Bryant, P. K., Rosemond, J., Scott, D. L., and Champness, J. N. (1999) 2.0 Å x-ray structure of the ternary complex of 7,8-dihydro-6-hydroxymethylpterin pyrophosphokinase from *Escherichia coli* with ATP and a substrate analogue. *FEBS Lett. 456*, 49–53.
12. Shi, G., Gao, J., and Yan, H. (1999) $^{1}H$, $^{13}C$ and $^{15}N$ resonance assignments of *Escherichia coli* 6-hydroxymethyl-7,8-dihydropterin pyrophosphokinase and its complex with mgamppcp. *J. Biomol. NMR 14*, 189–190.
13. Shi, G., Gong, Y., Savchenko, A., Zeikus, J. G., Xiao, B., Ji, X., and Yan, H. (2000) Dissecting the nucleotide binding properties of *Escherichia coli* 6-hydroxymethyl-7,8-dihydropterin pyrophosphokinase with fluorescent 3′(2)′-*O*-anthraniloyladenosine 5′-triphosphate. *Biochim. Biophys. Acta 1478*, 289–299.
14. Blaszczyk, J., Shi, G., Yan, H., and Ji, X. (2000) Catalytic center assembly of HPPK as revealed by the crystal structure of a ternary complex at 1.25 Å resolution. *Structure 8*, 1049–1058.
15. Bermingham, A., Bottomley, J. R., Primrose, W. U., and Derrick, J. P. (2000) Equilibrium and kinetic studies of substrate binding to 6-hydroxymethyl-7,8-dihydropterin pyrophosphokinase from *Escherichia coli*. *J. Biol. Chem. 275*, 17962–17967.
16. Xiao, B., Shi, G., Gao, J., Blaszczyk, J., Liu, Q., Ji, X., and Yan, H. (2001) Unusual conformational changes in 6-hydroxymethyl-7,8-dihydropterin pyrophosphokinase as revealed by x-ray crystallography and NMR. *J. Biol. Chem. 276*, 40274–40281.
17. Shi, G., Blaszczyk, J., Ji, X., and Yan, H. (2001) Bisubstrate analogue inhibitors of 6-hydroxymethyl-7,8-dihydropterin pyrophosphokinase: Synthesis and biochemical and crystallographic studies. *J. Med. Chem. 44*, 1364–1371.
18. Li, Y., Gong, Y., Shi, G., Blaszczyk, J., Ji, X., and Yan, H. (2002) Chemical transformation is not rate-limiting in the reaction catalyzed by *Escherichia coli* 6-hydroxymethyl-7,8-dihydropterin pyrophosphokinase. *Biochemistry 41*, 8777–8783.
19. Blaszczyk, J., Li, Y., Shi, G., Yan, H., and Ji, X. (2003) Dynamic roles of arginine residues 82 and 92 of *Escherichia coli* 6-hydroxymethyl-7,8-dihydropterin pyrophosphokinase: Crystallographic studies. *Biochemistry 42*, 1573–1580.
20. Li, Y., Wu, Y., Blaszczyk, J., Ji, X., and Yan, H. (2003) Catalytic roles of arginine residues 82 and 92 of *Escherichia coli* 6-hydroxymethyl-7,8-dihydropterin pyrophosphokinase: Site-directed mutagenesis and biochemical studies. *Biochemistry 42*, 1581–1588.
21. Blaszczyk, J., Shi, G., Li, Y., Yan, H., and Ji, X. (2004) Reaction trajectory of pyrophosphoryl transfer catalyzed by 6-hydroxymethyl-7,8-dihydropterin pyrophosphokinase. *Structure 12*, 467–475.
22. Blaszczyk, J., Li, Y., Wu, Y., Shi, G., Ji, X., and Yan, H. (2004) Essential roles of a dynamic loop in the catalysis of 6-hydroxymethyl-7,8-dihydropterin pyrophosphokinase. *Biochemistry 43*, 1469–1477.
23. Li, Y., Blaszczyk, J., Wu, Y., Shi, G., Ji, X., and Yan, H. (2005) Is the critical role of loop 3 of *Escherichia coli* 6-hydroxymethyl-7,8-dihydropterin pyrophosphokinase in catalysis due to loop-3 residues arginine-84 and tryptophan-89? Site-directed mutagenesis, biochemical, and crystallographic studies. *Biochemistry 44*, 8590–8599.
24. Li, G., Felczak, K., Shi, G., and Yan, H. (2006) Mechanism of the conformational transitions in 6-hydroxymethyl-7,8-dihydropterin pyrophosphokinase as revealed by NMR spectroscopy. *Biochemistry 45*, 12573–12581.
25. Marley, J., Lu, M., and Bracken, C. (2001) A method for efficient isotopic labeling of recombinant proteins. *J. Biomol. NMR 20*, 71–75.
26. Sattler, M., Schleucher, J., and Griesinger, C. (1999) Heteronuclear multidimensional NMR experiments for the structure determination of proteins in solution employing pulsed field gradients. *Prog. Nucl. Magn. Reson. Spectrosc. 34*, 93–158.
27. Delaglio, F., Grzesiek, S., Vuister, G. W., Zhu, G., Pfeifer, J., and Bax, A. (1995) Nmrpipe: A multidimensional spectral processing system based on Unix pipes. *J. Biomol. NMR 6*, 277–293.
28. Johnson, B. A., and Blevins, R. A. (1994) Nmrview: A computer program for the visualization and analysis of NMR data. *J. Biomol. NMR 4*, 603–614.
29. Farrow, N. A., Muhandiram, R., Singer, A. U., Pascal, S. M., Kay, C. M., Gish, G., Shoelson, S. E., Pawson, T., Forman Kay, J. D., and Kay, L. E. (1994) Backbone dynamics of a free and phosphopeptide-complexed *src* homology 2 domain studied by $^{15}N$ NMR relaxation. *Biochemistry 33*, 5984–6003.
30. Markley, J. L., Horsley, W. J., and Klein, M. P. (1971) Spin-lattice relaxation measurements in slowly relaxing complex spectra. *J. Chem. Phys. 55*, 3604–3605.
31. Fushman, D., Cahill, S., and Cowburn, D. (1997) The main-chain dynamics of the dynamin pleckstrin homology (ph) domain in solution: Analysis of N-15 relaxation with monomer/dimer equilibration. *J. Mol. Biol. 266*, 173–194.
32. Koradi, R., Billeter, M., and Wüthrich, K. (1996) Molmol: A program for display and analysis of macromolecular structures. *J. Mol. Graphics 14*, 51–55.
33. Walker, O., Varadan, R., and Fushman, D. (2004) Efficient and accurate determination of the overall rotational diffusion tensor of a molecule from N-15 relaxation data using computer program rotdif. *J. Magn. Reson. 168*, 336–345.
34. Dosset, P., Hus, J. C., Blackledge, M., and Marion, D. (2000) Efficient analysis of macromolecular rotational diffusion from heteronuclear relaxation data. *J. Biomol. NMR 16*, 23–28.
35. de la Torre, J. G., Huertas, M. L., and Carrasco, B. (2000) Hydronmr: Prediction of NMR relaxation of globular proteins from atomic-level structures and hydrodynamic calculations. *J. Magn. Reson. 147*, 138–146.
36. Lipari, G., and Szabo, A. (1982) Model-free approach to the interpretation of nuclear magnetic resonance relaxation in macromolecules. 2. Analysis of experimental results. *J. Am. Chem. Soc. 104*, 4559–4570.
37. Lipari, G., and Szabo, A. (1982) Model-free approach to the interpretation of nuclear magnetic resonance relaxation in macromolecules. 1. Theory and range of validity. *J. Am. Chem. Soc. 104*, 4546–4559.
38. Clore, G. M., Szabo, A., Bax, A., Kay, L. E., Driscoll, P. C., and Gronenborn, A. M. (1990) Deviations from the simple two-parameter model-free approach to the interpretation of N-15 nuclear magnetic-relaxation of proteins. *J. Am. Chem. Soc. 112*, 4989–4991.
39. Richey, D. P., and Brown, G. M. (1969) The biosynthesis of folic acid. IX. Purification and properties of the enzymes required for the formation of dihydropteroic acid. *J. Biol. Chem. 244*, 1582–1592.
40. Talarico, T. L., Dev, I. K., Dallas, W. S., Ferone, R., and Ray, P. H. (1991) Purification and partial characterization of 7,8-dihydro-6-hydroxymethylpterin-pyrophosphokinase and 7,8-dihydropteroate synthase from *Escherichia coli* MC4100. *J. Bacteriol. 173*, 7029–7032.
41. Talarico, T. L., Ray, P. H., Dev, I. K., Merrill, B. M., and Dallas, W. S. (1992) Cloning, sequence analysis, and overexpression of *Escherichia coli* folk, the gene coding for 7,8-dihydro-6-hydroxymethylpterin-pyrophosphokinase. *J. Bacteriol. 174*, 5971–5977.
42. Schurr, J. M., Babcock, H. P., and Fujimoto, B. S. (1994) A test of the model-free formulas—Effects of anisotropic rotational diffusion and dimerization. *J. Magn. Reson., Ser. B 105*, 211–224.
43. Åkerud, T., Thulin, E., Van Etten, R. L., and Akke, M. (2002) Intramolecular dynamics of low molecular weight protein tyrosine phosphatase in monomer-dimer equilibrium studied by NMR: A model for changes in dynamics upon target binding. *J. Mol. Biol. 322*, 137–152.
44. Palmer, A. G., Kroenke, C. D., and Loria, J. P. (2001) Nuclear magnetic resonance methods for quantifying microsecond-to-millisecond motions in biological macromolecules. *Methods Enzymol. 339*, 204–238.
45. DeLano, W. L. (2002) DeLano Scientific, Palo Alto, CA.

BI8016262